Materials Research. 2024; 27:e20240021
DOI: https://doi.org/10.1590/1980-5373-MR-2024-0021

Effect of Treatment Temperature on the Cyclic Spherical Contact Behavior of Plasma Nitrided and Nitrocarburized AISI 321 Steel

M.D. Manfrinato[a,b], L.S. Rossino[a,b], A.M. Kliauga[b], J. E. Escobar-Hernández[c], L. Melo-Máximo[d], G. A. Rodríguez-Castro[c], R. C. Morón[d*]

[a]*FATEC Sorocaba, Departamento de Metalurgia e Materiais, Sorocaba, SP, Brasil.*
[b]*Universidade Federal de São Carlos, Sorocaba, SP, Brasil.*
[c]*Instituto Politécnico Nacional, SEPI ESIME Zacatenco, Grupo Ingeniería de Superficies, U.P. Adolfo López Mateos, Zacatenco, Ciudad de México, 07738, México.*
[d]*Tecnológico Nacional de México / IT de Tlalnepantla, División de Estudios de Posgrado e Investigación, Av. Instituto Tecnológico S/N, Col. La Comunidad, Tlalnepantla de Baz, Estado de México, 54070, México.*

Received: January 17, 2024; Revised: April 13, 2024; Accepted: May 27, 2024

This work studied the cyclic spherical contact behavior of plasma nitrided (N) and nitrocarburized (NC) AISI 321 steel. The temperature and exposition time were 400 and 500 °C for 6 h in each treatment. A superficial hardness between ~10 (NC 400 °C) and ~17 GPa (NC 500 °C) was found by instrumented indentations; moreover, plastic and total work of indentation were analyzed. In cyclic spherical contact assessment, a critical load was first determined by applying tests between 100 and 1000 N. Next, cyclic tests were conducted with three subcritical loads (120, 150, and 180 N) and up to 10^5 cycles. A detrimental effect of treatment temperature was observed, 500 °C treatments presented worse failures than 400 °C, which is explained by the decomposition of expanded austenite. Between 400 °C treatments, nitrocarburizing presented a better performance, its higher plastic work of indentation is associated with a better energy absorption capacity.

Keywords: *Nitriding, nitrocarburizing, expanded austenite, contact fatigue, cyclic load, spherical contact.*

1. Introduction

Stainless steels are iron-base alloys containing a minimum of around 11% Cr; this element and oxygen form a protective chromium-rich oxide surface film[1]. Among different types of stainless steels, there is a group called austenitic stainless steels having a face-centered cubic (FCC) structure attributed to the use of austenite stabilizing elements like nickel, manganese, and nitrogen. In this group, chromium varies between 16 and 26%, nickel up to 35%, and manganese up to 15%[2]. Considering the total stainless steel production, austenitic stainless steel represents around 70% of the share[3]. These steels are widely employed in diverse industries, from food, nuclear, chemical, and power engineering to automotive and biomedical[4,5].

Among different stainless steel grades, AISI 321 is used for exhaust manifolds, pressure vessels, expansion bellows, stack liners, furnace parts, boilers, and chemical reactors[6-8]. However, its relatively low hardness and yield strength are insufficient for load-bearing demanding applications[7,9]. The surface of machine components manufactured of AISI 321 steel is subjected to cyclic stresses and temperatures, its working conditions include repeated contact interactions and low cycle fatigue[10,11].

Hence, different surface modification processes have been explored to improve the surface properties of stainless steels and overcome the drawbacks mentioned above; among them are thermochemical processes such as boriding, aluminizing, nitriding, or nitrocarburizing. In the first two, boron or aluminum atoms are diffused into the substrate, both treatments have received comprehensive coverage in the literature, and novel approaches continue being proposed[12-14]; they are conducted at high temperatures and may be insufficient to meet the tribological and cyclical needs in the case of aluminizing, or can affect the corrosion resistance of the steel, as has been previously reported for boriding[15]. On the other hand, nitriding is a thermochemical process where nitrogen atoms are introduced into the surface of a steel, causing minimal distortion due to the operating temperature. Whereas in nitrocarburizing, nitrogen and carbon atoms are diffused to the surface of the material, successively or simultaneously. Both processes increase surface hardness, wear resistance, and fatigue endurance[16,17]. Mainly, nitriding is conducted at temperatures between 400 and 590 °C, whereas nitrocarburizing is usually applied at ~550 to 590 °C. In nitriding, the microstructure is composed of Fe_4N (γ') and/or $Fe_{2-3}N$ (ε), and a diffusion zone is formed below; on the other hand, in nitrocarburizing the microstructure is Fe_4N

*e-mail: roberto.vm@tlalnepantla.tecnm.mx

(γ') and/or Fe_{2-3}[C, N] (ε) with a nitrogen-rich diffusion zone below it[17].

However, when nitriding or nitrocarburizing treatments are conducted on austenitic stainless steels at temperatures above 450 °C, their corrosion resistance is affected because CrN is produced and hinders the formation of the passive protective film due to the reduction of chromium in the layer[18]. Advantageously, both treatments can be conducted at low temperatures in different stainless steels, and the layers obtained are wear and corrosion-resistant[19]. Below a temperature of 450 °C occurs the formation of a precipitation-free layer called expanded austenite or S-phase (S)[4,5,18,20-23]; Borgioli has profoundly reviewed this phase[5,24]. When a stainless steel is subjected to a low-temperature treatment, interstitial atoms in the austenite lattice form a supersaturated solution, this does not occur in martensite or ferritic steels[5].

Currently, the literature lacks studies about the cyclic spherical contact behavior of AISI 321 steel subjected to nitriding or nitrocarburizing. Alfredsson & Olson proposed a methodology called standing contact fatigue (SCF) for assessing cyclic spherical contact, which comprises a spherical indenter repeatedly impacting a plane specimen in pure normal contact without lubrication, friction, or wear[25]. Previous SCF works have reported austenitic stainless steel (AISI 316L) subjected to nitriding only at 580 °C[26,27]. Hence, this work aimed to investigate the effect of lower treatment temperatures (400 and 500 °C) on the cyclic spherical contact performance of nitrided and nitrocarburized AISI 321 steel. In addition, microstructure analysis of the layers included scanning electronic microscopy (SEM) coupled with energy dispersive spectroscopy (EDS), and X-ray diffraction (XRD); Berkovich instrumented indentations were also conducted.

2. Methods

2.1. Thermochemical treatments and microstructure characterization

In this work, 6 mm thick samples of AISI 321 steel were cut from a 25.4 mm diameter bar, and Table 1 presents the nominal composition of this steel. The surface of the samples was prepared with SiC emery papers up to 2000 grit and then polished with 0.05 µm diamond paste to obtain a mirror finish. Before thermochemical treatments, the samples were ultrasonically cleaned with ethanol for 15 minutes. The reactor chamber for the plasma nitriding and nitrocarburizing treatments has been previously described[28]. First, a surface plasma cleaning was conducted, ablating for 1 h with argon (80%) and hydrogen (20%) gases at a pressure of 266.6 Pa; these parameters were chosen because they provide a high level of impurities removal[29]. Next, thermochemical treatments of nitriding and nitrocarburizing were conducted using the parameters given in Table 2. Four different layers were obtained, identified hereafter as: N400 - nitriding 400 °C, N500 - nitriding 500 °C, NC400 - nitrocarburizing 400 °C and NC500 - nitrocarburizing 500 °C.

Later, the samples were cross-sectioned to conduct a typical metallography procedure, using SiC emery papers up to 1500 grit and 1 µm diamond paste to obtain a mirror finish. Next, the micrographs were acquired by scanning electronic microscopy (JEOL, JSM-7800F) equipped with an energy-dispersive X-ray spectroscopy detector, from which a line elemental analysis profile along the depth of the layer was acquired. Further, the phases obtained in the thermochemical treatments were identified by X-ray diffraction tests (PANalytical, X'Pert3), using Cu-K_α radiation (λ = 0.154 nm) and 2θ range from 36 to 55°.

2.2. Instrumented indentation

Hardness (H) along the depth of the four layers was estimated by Berkovich indentations (CSM Instruments, TTX-NHT), with a load of 25 mN and load/unload rate of 50 mN·min^{-1}, analyzing the results by the Oliver and Pharr method[30]. Additionally, from the load-unload indentation curves, the total elastic work (W_T) and elastic work (W_E) values were obtained directly from CSM Indentation 4.16 software.

2.3. Standing contact fatigue tests

The standing contact fatigue tests were conducted with an electrodynamic test system (MTS Acumen), employing an alumina ball of 3 mm in diameter as the counterpart. This method comprised two steps. In the first, monotonic loads were perpendicularly applied to the sample surface, using a load range between 100 and 1000 N, with 100 N increments. Upon completion of this stage, failure mechanisms of the imprints were observed by optical microscopy (OM) to define and determine a critical load (P_{cr}) for specific cohesive damage. In particular, circumferential cracking was established as the failure criterion in this work.

Next, in the second step, cyclic (dynamic) tests with subcritical loads were conducted. These subcritical loads were set at 120, 150, and 180 N (40, 50, and 60% of the monotonic critical load), and the number of cycles was established between 10^3 and 10^5 using 5 Hz of frequency. Similarly, the overall set of footprints was inspected by OM, and some were analyzed by SEM.

Table 1. Nominal chemical composition (wt.%) of the AISI 321 steel.

C	Mn	Si	Cr	Ni	P	S	Ti	Fe
0.08	2.0	1.0	17.0 — 19.0	9.0 — 12.0	0.045	0.03	5×%C min	Balance

Table 2. Parameters used for plasma nitriding and nitrocarburizing AISI 321 steel.

Treatments	Gases Proportion (%)	Total Gas Flow (sccm)	Voltage (V)	Time (h)	Temperature (°C)
N400	$75\ N_2 + 25\ H_2$	1000	370	6	400
N500			420		500
NC400	$75\ N_2 + 22\ H_2 + 3\ CH_4$		450		400
NC500			540		500

3. Results and Discussion

3.1. Microstructure

Figure 1 presents the SEM micrographs of the four layers produced at temperatures of 400 and 500 °C on the surface of AISI 321 steel, whereas Table 3 gathers the total thicknesses measured for each layer. From thickness measurements, it can be seen that plasma nitriding and nitrocarburizing are controlled diffusion processes, when the treatment temperature increased from 400 to 500 °C, thicker layers were produced. When nitriding (Figure 1a)) is conducted on austenitic stainless steel at low temperatures, i.e., 400 °C, a supersaturated solid solution of interstitial atoms forms in the austenite lattice; this layer can appear as a single homogeneous layer in the micrographs and is called expanded austenite or S-phase[5]. From Figure 1b), it can be seen that a duplex expanded austenite layer was formed, this structure occurs when nitrocarburizing treatment is conducted at low temperatures (e.g. 400 °C), and two layers are identified: the top layer corresponds to the nitrogen-rich phase (γ_N), and the bottom layer to the carbon-rich phase (γ_C)[31,32]. Overall, the EDS line analysis of four treatments shows a higher presence of N along the layers formed. Particularly, the results of the nitrocarburized layer formed at 400 °C (Figure 1b) demonstrate the formation of a double layer, a higher N content was registered from the surface down to ~3.5 µm, observing a sudden drop then. Regarding the C presence, a decrease was observed from around 7.5 µm. For both nitrocarburizing treatments (NC400 and NC500), a slight C increment ahead of the N signal drop is observed; this has been called the "pushing effect" of nitrogen on carbon, nitrogen has a high solubility in austenite, which leads to high N levels near the surface and contributes to the carbon atoms mobility to the steel interior[33,34].

Table 3. The total thicknesses of the four layers.

Layer	Total thickness, µm
Nitriding 400 °C (N400)	21.1±0.6
Nitrocarburizing 400 °C (NC400)	9.3±0.4
Nitriding 500 °C (N500)	35.8±1
Nitrocarburizing 500 °C (NC500)	55.5±2.2

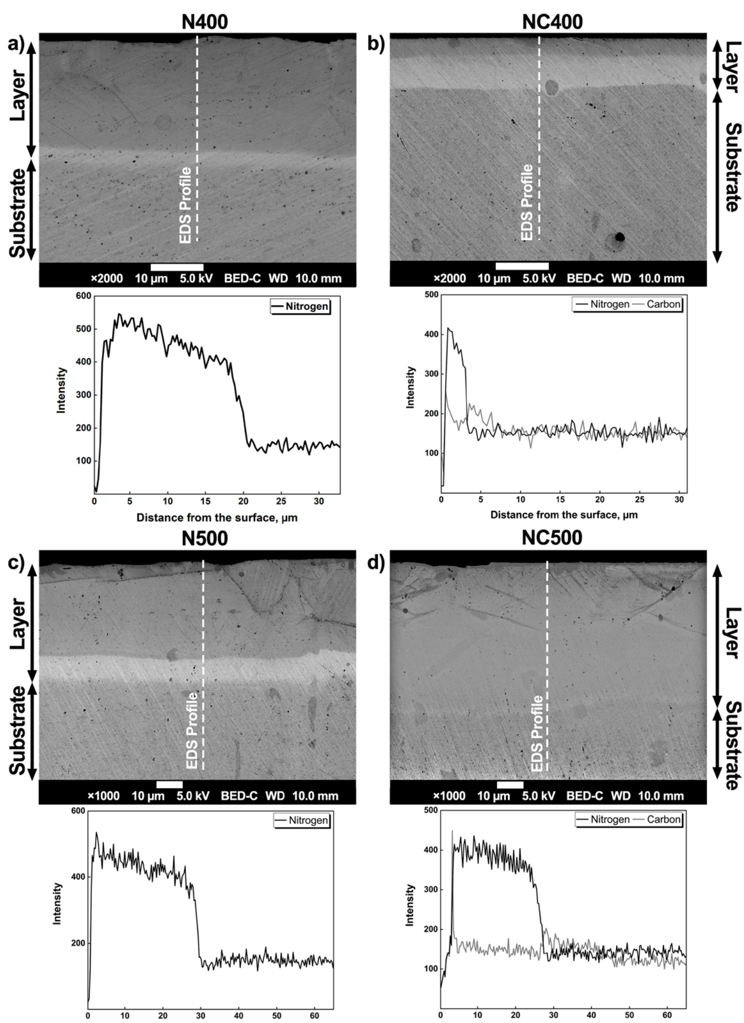

Figure 1. Micrographs and its corresponding EDS line analysis of the four layers a) nitriding 400 °C; b) nitrocarburizing 400 °C; c) nitriding 500 °C and d) nitrocarburizing 500 °C.

Figure 2 shows the XRD results, the layers formed at 400 °C are mainly composed of expanded austenite, S_N (N400) and $S_{C,N}$ (NC400). A displacement to lower angles is observed when the results of N400 and NC400 are compared with the diffraction pattern of AISI 321 steel; this shift, along with a characteristic broader peak, is associated with the lattice expansion due to interstitial dissolution of nitrogen or carbon. This lattice expansion is accommodated by compressive residual stresses in the expanded austenite phase[4,5,23,35,36]. Further, in 500 °C treatments, a change in the phase composition of the layers occurred. Expanded austenite is a metastable phase, so when the treatment temperature increases, S-phase decomposes, and there is a tendency to form nitride precipitates; thus, CrN, along with Fe_4N, are formed[20,24]. For these 500 °C treatments, S_N, CrN, and γ' (N500) and $S_{C,N}$, CrN and γ' (NC500) were identified. The formation of CrN in the layer decreases the weight percentage of the chromium element in the layer region, thus preventing the formation of the Cr_2O_3 film and decreasing corrosion resistance. The treatment temperature is the main parameter to avoid the precipitation of chromium nitrides and chromium carbides because substitutional diffusion is required, which only occurs above 500 °C[34,37].

3.2 Instrumented indentation results

Figure 3a) shows the hardness (H) results along the depth of four layers, all presented diffuse-type profiles, that is, hardness decreased as the distance from the surface increased. The inset depicts the load-displacement curves obtained at the first indentation in each sample, i.e., the closest indentations to the surface. For treatments at 400 °C, N400 reached around 15 GPa near the surface, whereas NC400 reached ~10 GPa. This can be related to the nitrogen detected in the layers, according to the EDS analysis of Figure 1b) (which employed the same acceleration voltage, magnification, and working distance on all the samples), the nitrogen signal detected at the surface of NC400 is lower than at the surface of N400 (Figure 1a)). Although nitrogen atomic radius is smaller than carbon, the effective size of nitrogen atoms in solid solution is larger, therefore larger distortion of the lattice is produced; nitrogen introduction in solid solution imparts solid solution strengthening of austenite[5,38]. Additionally, the lower hardness of NC400 might be explained by the occurrence of elastoplastic accommodation revealed through EBSD tests in carbon-expanded austenite; rotation of some grains in the lattice takes place due to plastic deformation[39]. Further, compressive residual stresses are linked to the expansion of the austenite lattice, which eventually impacts hardness[40,41]. Regarding 500 °C treatments, N500 reached around 15 GPa, whereas a value of ~17 GPa was registered for NC500. This hardness increase is explained by nitrogen content in the layer and the decomposition of expanded austenite into CrN and Fe_4N compounds, as XRD data shows (Figure 2), the formation of these phases is hindered at low temperature (400 °C) treatments. Regardless of treatment, a hardness between 3 and 4 GPa was estimated below the layers.

Figure 3b) presents the results of plastic work (W_P) and total work of indentation (W_T) along the depth of the layers. These results are extracted from the load-displacement curves obtained during indentation. The area under the loading curve represents the total work during indentation, and the area under the unloading curve represents elastic work of indentation (W_E); thus, the energy absorbed by

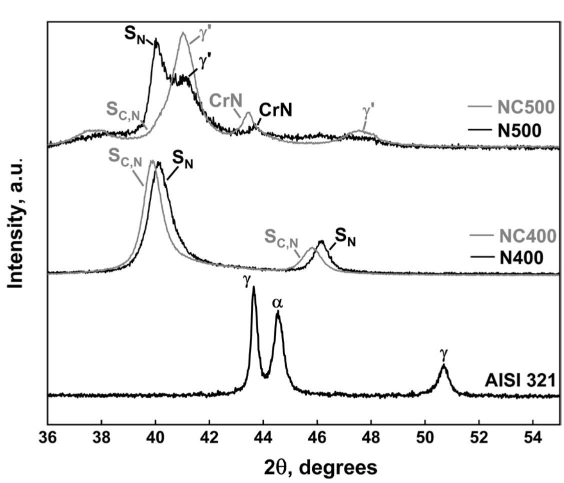

Figure 2. X-ray diffraction patterns obtained at the surface of the samples.

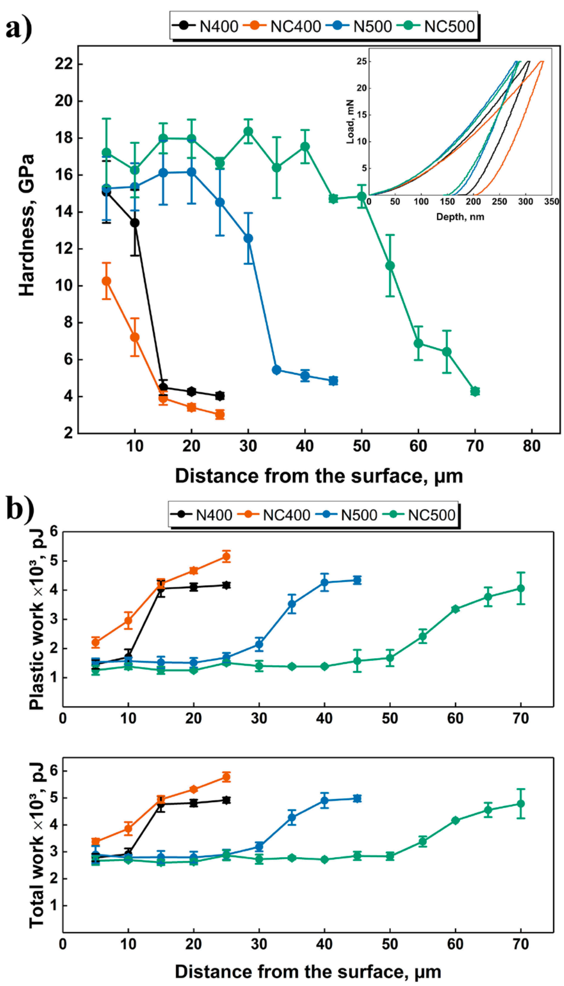

Figure 3. Instrumented indentation results: a) hardness; b) plastic and total work of indentation.

plastic deformation (plastic work) is estimated according to $W_P = W_T - W_E$[42,43]. The stored elastic energy within the sample is described by the plastic work (W_P)[44]. These work of indentation components are used to characterize plastic properties of materials[45], but can also be associated with SCF behavior of diffusion layers[46]. From these plots, it is seen that near the surface (~5 µm), NC400 presented the highest value of W_P, this trend above the other samples continues along the depth of the layer; this can be associated with a more ductile behavior, which is explained by its abovementioned phase composition. In contrast, NC500 presents lower values of W_P and W_T near the surface, closely followed by N400 and N500. Having a higher W_P is beneficial for SCF performance because it reveals a higher capacity for energy absorption; thus, the layer can better withstand the cyclic contact imposed by the alumina counterpart.

3.3. Standing contact fatigue

3.3.1. Monotonic tests

Figure 4 presents selected micrographs of the monotonic load tests overall layers, these were conducted with a normal load range between 100 and 1000 N, using 100 N increments. This step aimed to critical load identification, which is the normal load where reproducible cohesive damage is produced. In this work, circumferential cracking was established as the critical failure, the layer that presented the best integrity after the test was considered for critical load determination. Therefore, NC400 was chosen to establish the circumferential cracking appearance, and the same critical load was used for an adequate comparison among all layers. The 400 °C layers showed better integrity after being tested, the cohesive damage produced even with the highest load was only crack formation without spallations. The expanded austenite of N400 and NC400 presented a better absorption (see. Figure 3b)) of the mechanical load imposed by the alumina counterpart. Between N400 and NC400, the nitrocarburized layer presented a slightly better performance, a higher energy absorption capacity might be related to the residual stress state, which is being considered for further investigations.

In contrast, catastrophic failures were achieved with the monotonic tests applied in 500 °C layers. Even at the first stage, NC500 presented some spallations. This can be associated with the phase composition of 500 °C layers, where the decomposition of S occurred, leading to the formation of a harder, although more brittle CrN phase, plus Fe_4N. From Figure 3b) it can be observed that these 500 layers show lower W_P, which reveals a worse elastic energy absorption capacity. Even at the 300 N test, which was established as the critical load P_{CR}, the integrity of the N500 and NC500 layers was not satisfactory, because both conditions presented spallations, and these failures increased their magnitude up to the catastrophic failures seen with 1000 N.

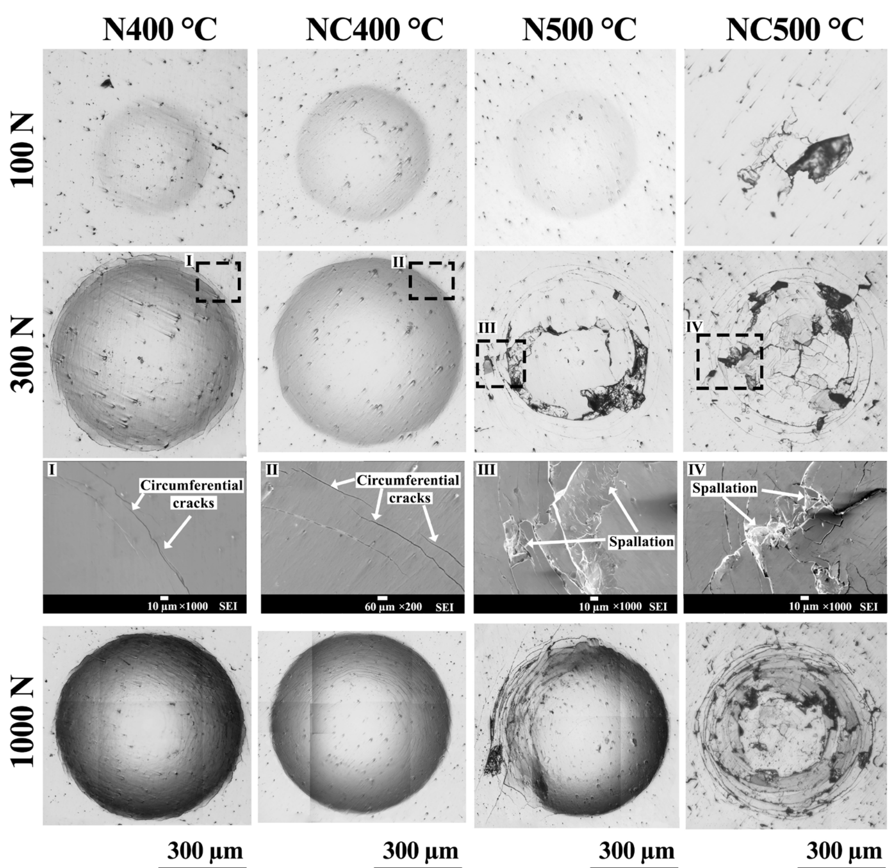

Figure 4. Monotonic load results at specific stages for all layers.

Figure 5 presents diameters (d) and depths (h) as functions of the normal load; this data was determined from the optical micrographs acquired for overall tests. The diameter was directly measured with the aid of ImagePro Plus 6.2 software, whereas theoretical depth was calculated from $h = d^2 \cdot R^{-1}$ (µm), where d (µm) is the diameter of the monotonic contact fatigue imprint, and R (µm) is the alumina ball radius (1.5 mm) employed as counterpart. It is clear that the imprints diameter linearly increased with the normal load. At the first and lower load, i.e., 100 N, the N500 layer presented the lowest diameter and depth, associated with its phase composition and instrumented indentation results; it shows high resistance to monotonic contact fatigue tests at low loads. Nonetheless, at the end of the load range, the N500 layer presented the largest diameter and depth, because of the catastrophic failure produced with 1000 N. Despite NC500 showing a lower depth and diameter after 1000 N tests, its integrity is compromised, as Figure 4 shows, so it was dismissed. Following NC500 in the lowest diameter and depth behavior is the NC400 layer, at the highest load, this layer reached a diameter of around 1970 µm and a depth of about 648 µm, so, considering its integrity after the tests, NC400 presented the best performance under monotonic load tests.

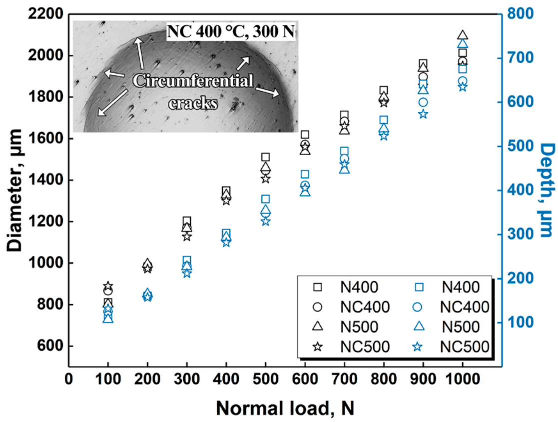

Figure 5. Diameter and residual depth as a function of normal load for all layers.

3.3.2. Cyclic load tests

After establishing 300 N as the critical load, tests between 10^3 and 10^5 cycles were conducted, applying three subcritical loads: 120 N (40%), 150 N (50%), and 180 N (60%) in each layer. The evolution of failure maps for NC400 and NC500 layers are depicted in Figures 6 and 7, only these maps are presented because they correspond to the best and worst performance layers, respectively. It can be seen that NC400 remarkably withstands the cyclic contact imposed overall experiments, even at the extreme conditions (180 N and 10^5 cycles), spallations were not produced on the layer, and only minor cracks at the contact periphery were observed. In contrast, the NC500 layer/substrate system could not absorb the elastic energy produced during the repeated indentations by the alumina sphere. Large circumferential cracks and minor spallations can be observed even at the initial contact fatigue condition (120 N and 10^3 cycles), and these failures increased in magnitude as the test conditions rose.

Circumferential cracks are normal to the sample and are formed at the edge of the contact, where a state of pure shear stress occurs when the alumina sphere is pressed against the surface. The radial stress component σ_r given by the Hertz solution

$$\sigma_r = \frac{1}{2}(1-2\nu)\,p_m$$

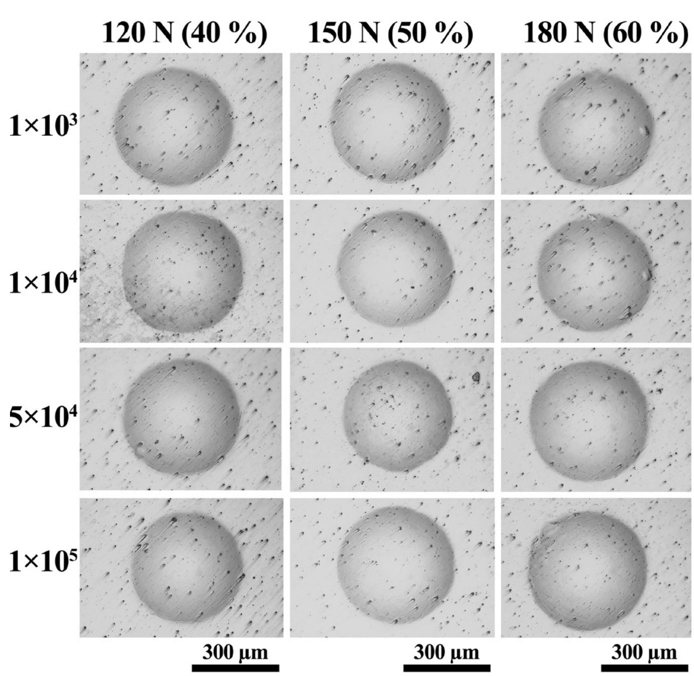

Figure 6. Evolution of cyclic contact imprints for nitrocarburized AISI 321 steel at 400 °C.

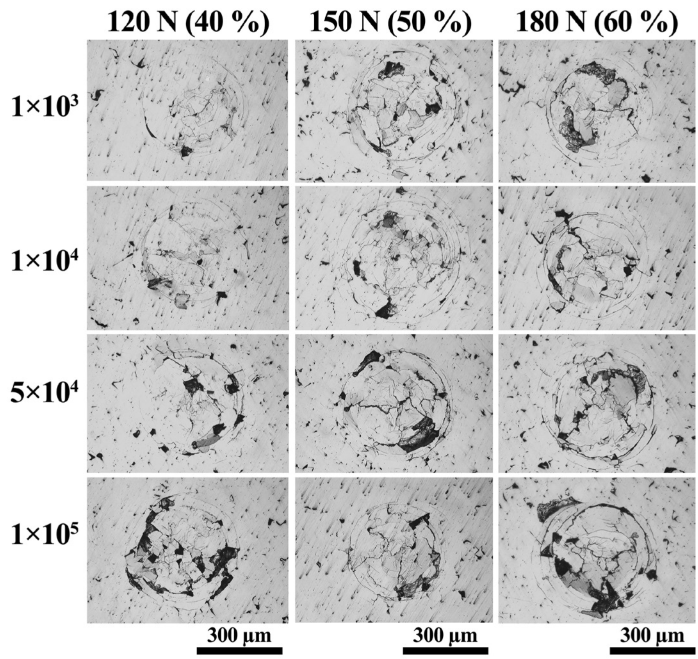

Figure 7. Evolution of cyclic contact imprints for nitrocarburized AISI 321 steel at 500 °C.

where p_m is the mean pressure and ν is the Poisson's ratio, is the maximum principal stress in spherical contact and is responsible for circumferential cracks formation[47].

Further, the elastic energy stored in the layer continuously increases with the number of cycles, up to the point that it overcomes the layer capacity for energy absorption and is then released, fracturing the layer and causing spallations[26,46]. According to the finite element simulation of Fernández-Valdés et al.[27], the damage in the area of contact between the alumina counterpart and the sample can be categorized in three zones: a central zone where compressive stresses are caused due to the contact of the pressing sphere and the sample, an intermediate zone close to the edge where the layer is subjected to bending and maximum principal stress is produced on the surface causing detachments of the layer, and a peripheral zone where the tensile radial stress produces circumferential cracking.

According to the results of instrumented indentation and contact fatigue tests, the treatment temperature adversely affected the performance of the layers. When the treatment temperature increased to 500 °C, expanded austenite S is decomposed, leading to the formation of CrN and Fe_4N; these phases exhibited a higher hardness in comparison to 400 °C layers; however, its capacity to absorb energy (W_P and W_T) decreased, this resulted in the formation of circumferential cracks and spallations in every stage of the cyclic tests.

Scanning electronic microscopy micrographs of the failure mechanisms produced on NC400 and NC500 layers are presented in Figure 8. It can be seen that NC400 layer at the highest number of cycles (10^5) showed high resistance to cyclic contact loading, under these experimental conditions, spallations were not produced nor circumferential cracking. The absence of significant cohesive damage around the contact area can be seen in the SEM details (Figure 8a)), where only some plastic deformation and cracks are seen. As for the NC500 imprints, a fractured layer can be seen even since the first stage (Figure 8b)), whereas in the extreme conditions (Figure 8c)) a heavily fractured layer is seen, its poor SCF performance is associated with a low energy absorption capacity.

Figure 9 depicts the damage observed during cyclical tests on four layers, considering different numbers of cycles and three subcritical loads. When cyclic loads are applied to the samples, the damage is higher than in monotonic loads alone. It can be seen that N400, NC500, and N500 were sensitive to the effect of cyclic loads, whereas NC400 flawlessly withstood the experimental conditions employed. For the N400 layer, circumferential cracks were observed after every stage analyzed. In contrast, NC400 presented a high resistance to cyclic loading, and after every test, no circumferential cracks or spallations were observed. Regarding N500, circumferential cracks started from the lowest load and number of cycles, increasing their severity until they became spallations; this latter failure was only observed at the highest subcritical load (180 N) and two stages: 5×10^4 and 1×10^5 cycles. Finally, the NC500 layer presented the worst cyclic loading behavior, spallations were observed from the first stage analyzed: 120 N of load and 1000 cycles. From Figure 9, it is concluded that temperature treatment had a determining effect on the contact fatigue performance of the layers. The layers formed at 400 °C presented a better performance than 500 °C layers; fractures and spallations were observed only in 500 °C layers. Contrastingly, the N400 layer presented circumferential cracks of lesser magnitude, and NC400 withstood the SCF tests without spallations or cracking, its higher W_P explains this performance. Summarizing, under the experimental conditions employed, 500 °C treatments are discarded because of their failure mechanisms; then,

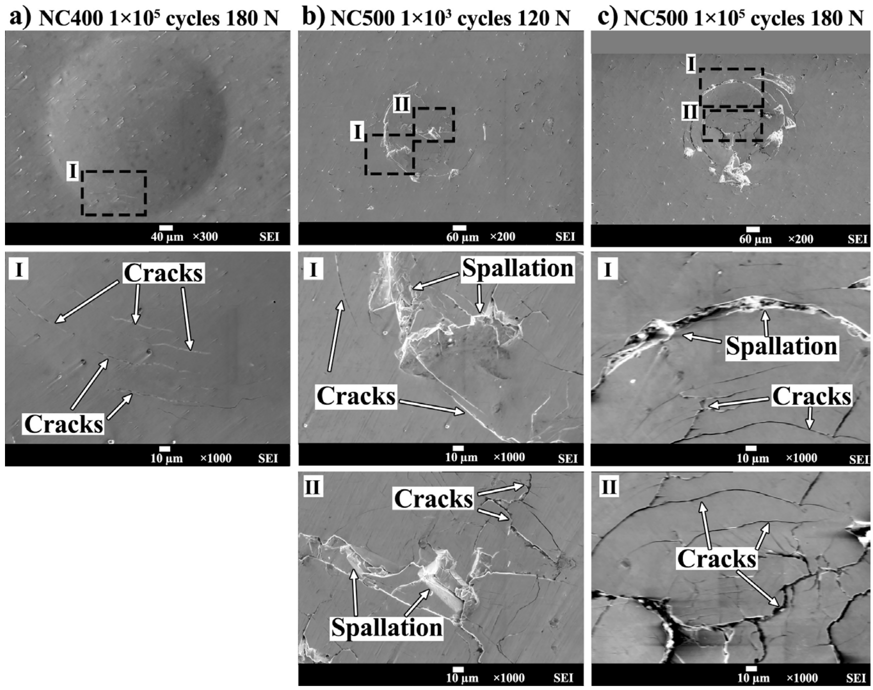

Figure 8. Failures produced at specific stages in a) NC 400 1×10^5 cycles 180 N; b) NC500 1×10^3 cycles 120 N; c) NC500 1×10^5 cycles 180 N.

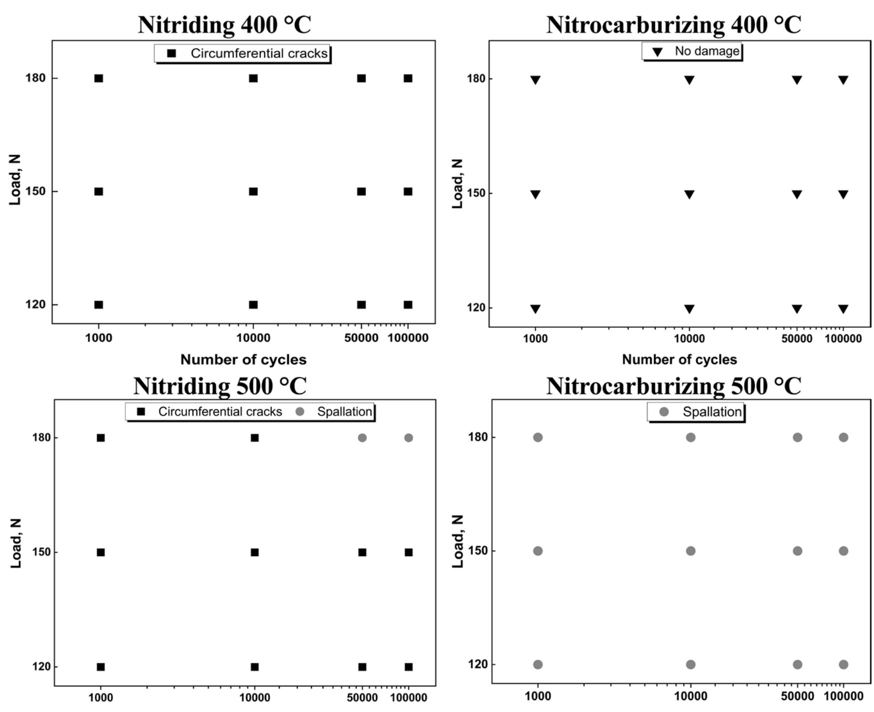

Figure 9. Diagram presenting the damage evolution under cyclic loading.

nitrocarburizing at 400 °C (NC400) presented a better cyclic contact fatigue performance over nitriding at 400 °C (N400). Figure 9 depicts how in the NC400 layer, no circumferential cracks were observed, this layer showed a high contact fatigue resistance, the imposed load was not able to produce even cohesive failures, and its higher capacity for energy absorption imparts this capability.

Finally, regarding the continuous search for the best cost-effective process for industrial applications, the energy consumption issue needed to conduct the 500 °C treatments is avoided because the nitrided and nitrocarburized layers formed at this temperature were unsatisfactory. Later, since both nitriding and nitrocarburizing are similar cost processes (the latter being only 2.59% more expensive), nitrocarburizing positions ahead of nitriding. The addition of carbon significantly helps with cyclical spherical contact fatigue resistance, as the results of this study show, the nitrocarburized layer is more ductile than the nitrided layer, therefore it can withstand higher plastic deformation without showing circumferential cracks or spallations.

4. Conclusions

According to the microstructural, mechanical and contact fatigue results, it can be concluded that

1. At a treatment temperature of 400 °C, the nitrided and nitrocarburized layers were composed of expanded austenite (S), whereas at 500 °C, the S phase decomposed, resulting in the identification of CrN and Fe_4N.
2. Increasing the treatment temperature to 500 °C resulted in higher hardness because CrN and Fe_4N phases were identified. However, this decreased its energy absorption capacity, the layers formed at 500 °C presented lower values of plastic (W_P) and total work of indentation (W_T).
3. When the treatment temperature increased from 400 to 500 °C, the standing contact fatigue performance was detrimentally affected. The layers formed at 400 °C showed better performance with less severe failures. In contrast, 500 °C layers presented critical fractures, even from the first stage in NC500.
4. Between N400 and NC400, the nitrocarburized layer presented a better performance, maintaining its integrity even after all standing contact fatigue tests. This is associated with its higher plastic work (W_P), which allows a better energy absorption capacity, explaining the absence of circumferential cracks under the experimental conditions employed.

5. Acknowledgments

The authors gratefully acknowledge Dr. Hugo Martínez Gutiérrez and Dr. Israel Arzate Vázquez at Centro de Nanociencias y Micro y Nanotecnologías (CNMN IPN) for SEM/EDS and instrumented indentations, respectively.

6. References

1. Davis JR. ASM Specialty Handbook Stainless Steels. Materials Park, OH: ASM International; 1994. 576 p.
2. ASM Handbook Committee. ASM Handbook. Vol. 1: Properties and Selection: Irons, Steels, and High-Performance Alloys. Materials Park, OH: ASM International; 1990. 1063 p.
3. Günen A, Karakaş MS, Kurt B, Çalik A. Corrosion behavior of borided AISI 304 austenitic stainless steel. Anti-Corros Methods Mater. 2014;61(2):112-9.
4. Sah J, Joseph A, Jhala G, Mukherjee S. On the effects of H2 and Ar on dual layer formed by plasma nitrocarburizing on austenitic stainless steels. J Mater Eng Perform. 2022;31(4):2664-77.
5. Borgioli F. The “expanded” phases in the low-temperature treated stainless steels: a review. Metals (Basel). 2022;12(2):331.
6. Nkhoma RKC, Siyasiya CW, Stumpf WE. Hot workability of AISI 321 and AISI 304 austenitic stainless steels. J Alloys Compd. 2014;595:103-12.
7. Tiamiyu AA, Eskandari M, Nezakat M, Wang X, Szpunar JA, Odeshi AG. A comparative study of the compressive behaviour of AISI 321 austenitic stainless steel under quasi-static and dynamic shock loading. Mater Des. 2016;112:309-19.
8. Li W, Chen H, Li C, Huang W, Chen J, Zuo L, et al. Microstructure and tensile properties of AISI 321 stainless steel with aluminizing and annealing treatment. Mater Des. 2021;205:109729.
9. Wang J, Lin Y, Yan J, Zen D, Zhang Q, Huang R, et al. Influence of time on the microstructure of AISI 321 austenitic stainless steel in salt bath nitriding. Surf Coat Tech. 2012;206(15):3399-404.
10. Savrai RA, Makarov AV, Osintseva AL, Malygina IY. Estimating the contact endurance of the AISI 321 stainless steel under contact gigacycle fatigue tests. J Mater Eng Perform. 2018;27(2):601-11.
11. Li W, Yang L, Li C, Chen H, Zuo L, Li Y, et al. Low-cycle fatigue and fracture behavior of aluminized stainless steel AISI 321 for solar thermal power generation systems. Metals (Basel). 2020;10(8):1-17.
12. Günen A, Gürol U, Koçak M, Çam G. A new approach to improve some properties of wire arc additively manufactured stainless steel components: simultaneous homogenization and boriding. Surf Coatings Technol. 2023;460:129395.
13. Campos-Silva I, Hernández-Ramirez EJ, Contreras-Hernández A, Rosales-Lopez JL, Valdez-Zayas E, Mejía-Caballero I, et al. Pulsed-DC powder-pack boriding: growth kinetics of boride layers on an AISI 316 L stainless steel and Inconel 718 superalloy. Surf Coatings Technol. 2021;421:127404.
14. Gürol U, Altınay Y, Günen A, Bölükbaşı ÖS, Koçak M, Çam G. Effect of powder-pack aluminizing on microstructure and oxidation resistance of wire arc additively manufactured stainless steels. Surf Coatings Technol. 2023;468:129742.
15. Mejía-Caballero I, Palomar-Pardavé M, Martínez Trinidad J, Romero-Romo M, Pérez Pasten-Borja R, Lartundo-Rojas L, et al. Corrosion behavior of AISI 316L borided and non-borided steels immersed in a simulated body fluid solution. Surf Coat Tech. 2015;280:384-95.
16. Davis JR. Surface hardening of steels: understanding the basics. Materials Park, OH: ASM International; 2002. 318 p.
17. Dearnley PA. Introduction to surface engineering. Cambridge: Cambridge University Press; 2017. Surface engineering with diffusion technologies; p. 35-115.
18. Alphonsa J, Raja VS, Mukherjee S. Study of plasma nitriding and nitrocarburizing for higher corrosion resistance and hardness of 2205 duplex stainless steel. Corros Sci. 2015;100:121-32.
19. Somers MAJ, Christiansen TL. Low temperature surface hardening of stainless steel. In: Mittemeijer EJ, Somers MAJ, editors. Thermochemical surface engineering of steels. USA: Elsevier; 2015. p. 557-79.
20. Larisch B, Brusky U, Spies HJ. Plasma nitriding of stainless steels at low temperatures. Surf Coat Tech. 1999;116-119:205-11.
21. Cheng Z, Li CX, Dong H, Bell T. Low temperature plasma nitrocarburising of AISI 316 austenitic stainless steel. Surf Coat Tech. 2005;191(2–3):195-200.
22. Mendes AF, Scheuer CJ, Joanidis IL, Cardoso RP, Mafra M, Klein AN, et al. Low-temperature plasma nitriding of sintered PIM 316L austenitic stainless steel. Mater Res. 2014;17:100-8.
23. Adachi S, Egawa M, Yamaguchi T, Ueda N. Low-temperature plasma nitriding for austenitic stainless steel layers with various nickel contents fabricated via direct laser metal deposition. Coatings. 2020;10(4):365.
24. Borgioli F. From austenitic stainless steel to expanded austenite-s phase: formation, characteristics and properties of an elusive metastable phase. Metals (Basel). 2020;10(2):187.
25. Alfredsson B, Olsson M. Standing contact fatigue. Fatigue Fract Eng Mater Struct. 1999;22(3):225-37.
26. Fernández-Valdés D, Meneses-Amador A, Rodríguez-Castro GA, Arzate-Vázquez I, Campos-Silva I, Nava-Sánchez JL. Standing contact fatigue behavior of nitrided AISI 316L steels. Surf Coat Tech. 2019;377:124871.
27. Fernández-Valdés D, Vidal-Torres J, López-Liévano A, Meneses-Amador A, López-García C, Rodríguez-Castro GA. Evaluation

of adhesive damage in a nitrided stainless steel under cyclic contact loading. Surf Coatings Technol. 2023;474:130101.
28. Da Cruz D, de Souza BA, de Campos L AP, de Almeida LS, Moreto JA, Manfrinato MD, et al. Projeto, construção e comissionamento de um reator para tratamento de nitretação iônica a plasma em aço P20. Rev Bras Apl Vácuo. 2019;37(3):102.
29. de Campos L de AP, de Almeida LS, da Silva BP, Danelon MR, Aoki IV, Manfrinato MD, et al. Evaluation of nitriding, nitrocarburizing, organosilicon interlayer, diamond-like carbon film and duplex plasma treatment in the wear and corrosion resistance of AISI 4340 steel. J Mater Eng Perform. 2020;29(12):8107-21.
30. Oliver WC, Pharr GM. An improved technique for determining hardness and elastic modulus using load and displacement sensing indentation experiments. J Mater Res. 1992;7(06):1564-83.
31. Dalke A, Burlacov I, Hamann S, Puth A, Böcker J, Spies H-J, et al. Solid carbon active screen plasma nitrocarburizing of AISI 316L stainless steel: influence of N2-H2 gas composition on structure and properties of expanded austenite. Surf Coat Tech. 2019;357(1):1060-8.
32. Cisquini P, Ramos SV, Lins VFC, Franco AR, Vieira EA. Micro-abrasive wear resistance of the duplex expanded austenite layer phases produced by plasma nitrocarburizing. Wear. 2019;436-437:203039.
33. Czerwiec T, He H, Marcos G, Thiriet T, Weber S, Michel H. Fundamental and Innovations in Plasma Assisted Diffusion of Nitrogen and Carbon in Austenitic Stainless Steels and Related Alloys. Plasma Process Polym. 2009;6(6-7):401-9.
34. Lee I. The effect of molybdenum on the characteristics of surface layers of low temperature plasma nitrocarburized austenitic stainless steel. Curr Appl Phys. 2009;9(3):S257-61.
35. Celik O, Baydogan M, Atar E, Kayali ES, Cimenoglu H. Fatigue performance of low temperature nitrided AISI 321 grade austenitic stainless steel. Mater Sci Eng A. 2013;565:38-43.
36. Somers MAJ, Christiansen TL, Winther G. Expanded austenite; from fundamental understanding to predicting composition- and stress-depth profiles. In: Proceedings of the European Conference on Heat Treatment (ECHT 2018); 2018; Friedrichshafen, Germany. Proceedings. USA: Elsevier; 2018. p. 91-101.
37. Tschiptschin AP, Pinedo CE. Surface hardening of stainless steel. In: Singh A, editor. Stainless steels. London: IntechOpen; 2022. p. 13.
38. Funch CV, Somlo K, Christiansen TL, Somers MAJ. Thermochemical post-processing of additively manufactured austenitic stainless steel. Surf Coat Tech. 2022;441:128495.
39. Werner KV., Che HL, Lei MK, Christiansen TL, Somers MAJ. Low temperature carburizing of stainless steels and the development of carbon expanded austenite. HTM - J Heat Treat Mater. 2022;77(1):3-15.
40. Somers MAJ. Development of compound layer and diffusion zone during nitriding and nitrocarburizing of iron and steels. In: Hashmi S, Batalha GF, van Tyne CJ, Yilbas B. Comprehensive materials processing. USA: Elsevier; 2014. p. 413-37.
41. Stinville JC, Tromas C, Villechaise P, Templier C. Anisotropy changes in hardness and indentation modulus induced by plasma nitriding of 316L polycrystalline stainless steel. Scr Mater. 2011;64(1):37-40.
42. Jha KK, Zhang S, Suksawang N, Lo Wang T, Agarwal A. Work-of-indentation as a means to characterize indenter geometry and load-displacement response of a material. J Phys D Appl Phys. 2013;46(41)
43. Tuck JR, Korsunsky AM, Bull SJ, Davidson RI. On the application of the work-of-indentation approach to depth-sensing indentation experiments in coated systems. Surf Coat Tech. 2001;137(2-3):217-24.
44. Fischer-Cripps AC. Nanoindentation. New York: Springer; 2004. Analysis of nanoindentation test data; p. 39-68.
45. Menčík J. Determination of mechanical properties by instrumented indentation. Meccanica. 2007;42(1):19-29.
46. Escobar-Hernández J, Rodríguez-Castro GA, Arzate-Vázquez I, Meneses-Amador A, Morón RC. Fatigue damage assessment from cyclic spherical contact of borided and nitrided H13 steel. Mater Lett. 2021;285:129118.
47. Abudaia FB, Evans JT, Shaw BA. Spherical indentation fatigue cracking. Mater Sci Eng A. 2005;391(1-2):181-7.